Convective Forcing of the North American Monsoon Anticyclone at Intraseasonal and Interannual Time Scales

KAI-WEI CHANG,[a] KENNETH P. BOWMAN,[a] LEONG WAI SIU,[b] AND ANITA D. RAPP[a]

[a] *Department of Atmospheric Sciences, Texas A&M University, College Station, Texas*
[b] *Department of Earth and Atmospheric Sciences, Cornell University, Ithaca, New York*

(Manuscript received 13 January 2021, in final form 16 June 2021)

ABSTRACT: In the upper troposphere and lower stratosphere (UTLS), large-scale anticyclones associated with monsoons play major roles in tropospheric and stratospheric transport and mixing. To understand the forcing of the North American monsoon anticyclone (NAMA), this study examines the connection between precipitation over the tropics and subtropics of the North American longitude sector and the variability of the troposphere and lower stratosphere. Using ERA5 and outgoing longwave radiation (OLR) data from 1979 to 2019, we assess the relationship at the intraseasonal time scale using pentad-mean time series. We show that OLR anomalies are correlated with circulation anomalies northwest and northeast of the region of precipitation. Decreased OLR (increased precipitation) corresponds to increased geopotential heights and anticyclonic circulation anomalies in the 300–100-hPa layer and an opposite response in the lower-tropospheric 850–600-hPa layer. The results are consistent with the established theory of the Rossby wave response to latent heating. The increase in height, which is strongest near 150 hPa, indicates that increased precipitation is associated with a strengthened NAMA. UTLS temperatures also have significant correlations with OLR, with cold (warm) anomalies occurring above (below) the core of the anticyclonic anomaly consistent with large-scale balance. The vertical structure of geopotential and temperature anomalies is compared to simulations using an idealized general circulation model, which shows that such a vertical structure is a consistent response to diabatic heating. Correlations at the interannual time scale resemble those at the intraseasonal time scale, demonstrating that precipitation is related to the NAMA at both time scales.

KEYWORDS: North America; Rossby waves; Stratospheric circulation; Anticyclones; Diabatic heating; Monsoons; Precipitation; Stratosphere; Upper troposphere; Latent heating/cooling; Interannual variability; Subseasonal variability

1. Introduction

The circulation of the upper troposphere and lower stratosphere (UTLS) affects the composition of lower-stratospheric air by controlling the location and rate of stratosphere-troposphere exchange. The diabatic heating and divergence associated with tropical and subtropical convection force large-scale waves that form quasi-stationary anticyclones (Matsuno 1966; Webster 1972; Gill 1980; Lau and Lim 1982) in the UTLS and also modulate the distribution of tropopause height in the subtropics and midlatitudes (Highwood and Hoskins 1998). During boreal summer, the Asian monsoon anticyclone (AMA) and the North American monsoon anticyclone (NAMA) are observed in the Northern Hemisphere, with the former being the dominant feature in the global UTLS circulation (Dunkerton 1995). The smaller scale of the NAMA is likely attributable to the smaller horizontal scale and intensity of the North American monsoon (NAM) (Tang and Reiter 1984), the weaker diabatic heating associated with the NAM (Hoskins and Rodwell 1995), and the different latitudinal distribution of the heating (Siu and Bowman 2019).

Both anticyclones are associated with high water vapor mixing ratio (Gettelman et al. 2004; Randel et al. 2015) and play important roles in transporting and mixing tropospheric air into the lower stratosphere (Dethof et al. 1999; Ploeger et al. 2013). The AMA is an important source of stratospheric air as tropospheric air injected into the AMA is often transported into the tropical pipe (Garny and Randel 2016). Likewise, the NAMA influences the transport and mixing in the UTLS over the Western Hemisphere (Pittman et al. 2007; Clapp et al. 2019). Because the circulation associated with the NAMA can significantly influence the composition of stratospheric air, it is necessary to understand how the NAMA is formed and the factors controlling its variability.

Hoskins and Rodwell (1995) showed that a realistic AMA can be simulated as the linear response to imposed heating. Garny and Randel (2013) used reanalysis and satellite observations to demonstrate the connection between AMA strength and convection. Precipitation from the NAM has been demonstrated to be related to the upper-tropospheric circulation (Higgins et al. 1997; Higgins and Shi 2001), and the position of the 500-hPa anticyclone is related to spatial shifts of precipitation in the southwestern United States (Diem and Brown 2009; Diem et al. 2013). Although it is not clear whether variations in precipitation directly cause shifts of the anticyclone position, Siu and Bowman (2019) showed that both the AMA and NAMA can be modeled as a response to diabatic heating, suggesting that a connection between latent heating from precipitation and anticyclone formation should exist. Stensrud (2013) conducted a case study using the Weather Research and Forecasting (WRF) Model and found that NAM deep convection is a source of stationary wave trains and upper-tropospheric positive geopotential height anomalies over northwestern

Corresponding author: Kai-Wei Chang, kwchang30@tamu.edu

DOI: 10.1175/JAS-D-21-0009.1

Mexico and the northeastern United States. However, the connection between diabatic heating and the NAMA has not been demonstrated with observations. In this study, we examine the relationship between NAMA strength and precipitation associated with the NAM using reanalysis and satellite datasets.

Typically, the onset phase of the NAM occurs in June, and its decay phase begins in September. Northwestern Mexico and the southwestern United States subsequently receive a large fraction of their annual rainfall in July and August (Adams and Comrie 1997), during which the NAM is in its mature phase. Mean July–August precipitation rates for 2000–19 are shown in Fig. 1. This monsoonal precipitation accounts for over 70% of annual rainfall over the Sierra Madre Occidental (Douglas et al. 1993). Following the onset of the NAM in June, precipitation over northwestern Mexico is relatively constant in July and August (Barlow et al. 1998), potentially acting as a quasi-steady heat source forcing the NAMA. Outside the NAM system, the intertropical convergence zone (ITCZ) may also influence the upper-tropospheric circulation. The role of each region's precipitation in modulating the NAMA is not well understood, nor has it been demonstrated that a connection exists at all. To improve the understanding of how precipitation influences the large-scale dynamics in the North American region, we utilize reanalysis and satellite datasets to explore whether there is evidence of atmospheric response to latent heating in observations. In this study we analyze how precipitation relates to the atmospheric circulation and temperature through correlation analyses at the intraseasonal and interannual time scales.

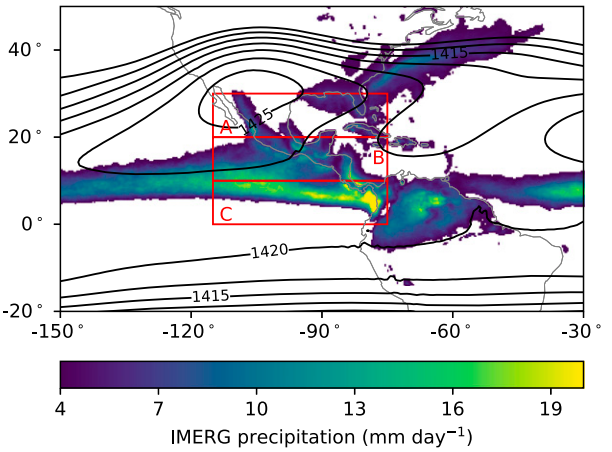

FIG. 1. 2000–19 IMERG July–August mean precipitation rate (colors) and 150-hPa ERA5 geopotential height (black; contour interval: 5 dam). Red boxes indicate the averaging regions A, B, and C used to compute pentad-mean OLR and precipitation-rate time series.

2. Data and analysis method

a. ERA5

ERA5 (Hersbach et al. 2020), the fifth-generation reanalysis from the European Centre for Medium-Range Weather Forecasts (ECMWF), is based on the Integrated Forecasting System (IFS) Cy41r2, and has a native resolution of TL639 (31 km) and 137 hybrid sigma–pressure levels. We use the pressure-level hourly geopotential height and temperature fields at 0.75° × 0.75° spatial resolution. Our analyses use the 23 pressure levels between 50 and 850 hPa. A total of 41 years (1979–2019) are used in this study.

b. NOAA interpolated OLR

The National Oceanic and Atmospheric Administration (NOAA) interpolated OLR dataset (Liebmann and Smith 1996) provides estimates of OLR dating back to June 1974. It is based on observations from NOAA polar-orbiting satellites and provides OLR estimates at 2.5° × 2.5° resolution. We use the daily mean dataset from 1979 to 2019 to make pentad time series, and the monthly mean dataset for the analyses at interannual time scales.

c. IMERG precipitation retrievals

The Integrated Multisatellite Retrievals for GPM (IMERG) (Huffman et al. 2018) algorithm provides precipitation rates by merging measurements from the Global Precipitation Mission (Hou et al. 2014) and the Tropical Rainfall Measurement Mission (TRMM) (Simpson et al. 1988) with various infrared and microwave observations from a suite of other low-Earth-orbiting and geostationary satellites. We use version 6 of the GPM_3IMERGDF Level 3 Final Precipitation product, which provides daily estimates of precipitation rate at 0.1° × 0.1° resolution. The GPM_3IMERGDF data from 2000 to 2019 are used to compute pentad time series for the correlation analysis in section 3a.

d. Lagged correlation using pentad time series

To explore the atmospheric response to diabatic heating from precipitation, we correlate ERA5 variables to either OLR or precipitation retrievals from IMERG. At each ERA5 grid point, pentad-mean time series are constructed for mid-June to mid-September of each year in 1979–2019; the pentads are centered on 17 June, 22 June, . . . , 10 September, making a total of 18 pentad periods per year. The 18 pentads from each year are concatenated to form a time series with 738 pentads. The time series are deseasonalized by removing the climatological mean of each pentad period, and then detrended using a linear regression fit.

Pentad-mean time series of OLR are made by performing area-weighted averaging over the boxed regions shown in Fig. 1. Section 3a uses OLR averages over the domain 0°–30°N, 115°–75°W (total area covered by boxes A, B, and C), while section 3c discusses correlations for the individual boxes. Boxes A, B, and C cover the same longitudinal and latitudinal and extent (40° × 10°). Since the atmospheric response has been shown to be dependent on the latitude of the forcing (Lau and Lim 1982; Siu and Bowman 2019), this analysis can elucidate the role of forcing at different latitudes.

The pentad periods of the OLR time series are shifted relative to those of ERA5 to obtain lagged correlations. For instance, to

evaluate the lag +1 (OLR precedes ERA5 variables by 1 day) correlations, pentad periods for the OLR time series are centered on 16 June, 21 June, . . . , 9 September of each year in 1979–2019. This time series is then correlated to the ERA5 time series at each ERA5 grid point to obtain the spatial distribution of lag +1 correlations. Although the time series are not continuous in time, we avoid correlating across years (e.g., correlating 9 September 1979–17 June 1980) since both the ERA5 and OLR/precipitation time series have 18 pentads from each year.

Time series of IMERG precipitation are made in the same way as OLR, but for the period 2000–19 only. OLR pentad time series contain 738 pentads (18 per year through 1979–2019) while IMERG time series contain 360 pentads (2000–19).

Linear regressions of the following form:

$$y_i = mx_i + b + \epsilon_i, \tag{1}$$

are computed, where the predictor x_i is pentad-mean OLR or precipitation, the predictand y_i is a lagged ERA5 variable, m is the slope, b is the intercept, ϵ_i is the regression error, and the subscript i is the observation index. Both variables are deseasonalized and detrended. The correlation coefficient r is also computed. Statistical testing of r is done by evaluating the effective degrees of freedom using the lag-1 autocorrelation (Bretherton et al. 1999) of the individual OLR and ERA5 time series, and then using the effective degrees of freedom in the two-tailed Student's t test.

3. Results

a. Three-dimensional structure of lagged correlations

Figure 2 shows the correlation coefficient r and the slope m of the linear regression of −OLR with respect to pentad-averaged ERA5 geopotential height at 150 and 700 hPa. The negative of the OLR is used because increased precipitation is associated with higher and colder cloud tops and reduced OLR. Therefore positive r and positive m indicate higher geopotential height (for example) in response to increased precipitation. In this figure the OLR values used are the mean inside all three regions in Fig. 1 (A + B + C). Each row of Fig. 2 shows r and m for different lags, which are given on the left side of the figure. At 150 hPa, there is a large region of positive r centered near 25°N, 130°W. The correlation here reaches a maximum with $r > 0.4$ at lag +6 days (i.e., geopotential height lags OLR by 6 days). The positive correlation suggests that positive precipitation anomalies tend to be followed by positive height anomalies in that region, which corresponds to anticyclonic flow anomalies. The lag +6, 150-hPa panel clearly shows that the strong positive height correlations are west of the climatological anticyclone. This will be discussed further in section 3d. A smaller region of significant correlations is also visible along the eastern coast of North America. Both regions are consistent with the Rossby wave trains diagnosed by Stensrud (2013) in a model initial-value experiment, which is discussed further below.

The standard deviations of the OLR pentad time series are shown in Table 1. For region A + B + C, the standard deviation of the OLR time series is 7.01 W m^{-2}. In the core of the anticyclonic anomaly at lag +6 in Fig. 2, m is slightly above 4 m (W m^{-2})$^{-1}$, indicating that the geopotential height anomaly would be ~28 m if the OLR is anomalously low by one standard deviation.

Correlations at 700 hPa (right column of Fig. 2) show the presence of reduced geopotential heights (negative r and m), corresponding to a cyclonic circulation anomaly, centered near 20°N, 120°W. At 700 hPa, the maximum magnitude of r occurs earlier than at 150 hPa; at a lag of 3 days, a region with $r < -0.6$ covers a large area. Details of the timing of maximum r are discussed in the next paragraph. Another difference with the 150-hPa level is that the cyclonic anomaly at 700 hPa tends to be located closer to the OLR box, that is, east and south of the upper-tropospheric anomaly. Also, the magnitude of r (~0.6) in the local extremum is higher at 700 hPa than at 150 hPa (~0.4).

The dependence of r on lag is displayed in more detail in Fig. 3, which shows the largest value of $|r|$ in 0°–60°N, 180°W–0°. The domain is limited to the Western Hemisphere north of the equator because the primary subject of interest is the circulation associated with the NAMA. Table 2 denotes the lags at which $|r|$ peaks at each pressure level as well as the locations where these values occur. In the upper troposphere (100–300 hPa) the locations of peak $|r|$ fall within 29°–30°N, 135°–140°W, while those in 400–850 hPa fall within 16°–19°N, 110°–113°W, so it confirms that the peak $|r|$ reflect the positions of the anomalies in Fig. 2.

At 100–300 hPa, the maximum $|r|$ occurs at a lag of 7 days. This is comparable to the results of Randel and Park (2006), who studied the connection between convection over Southeast Asia and the size of the AMA. They found a strong correlation between OLR and the area of low PV at isentropic levels between 340 and 370 K, with maximum correlations for lags around 5 days (cf. their Fig. 5). In the 400–850-hPa layer, we found that the strongest correlations are negative, with the largest magnitudes at lags of 1–2 days. This indicates that cyclonic anomalies in the midtroposphere occur after positive precipitation anomalies. The fact that OLR anomalies lead height anomalies supports the hypothesis that the geopotential height is responding to precipitation anomalies. Additionally, the observations indicate that the forced upper-tropospheric anticyclonic gyre forms later in time compared to the mid- to lower-tropospheric cyclonic anomaly.

Hovmöller plots of r for 150-hPa geopotential height are shown in Fig. 4a for 24.75°N, which approximately coincides with the local maximum of r at 150 hPa. The $r = 0.4$ contour appears around lag +4 days, disappears around lag +8, and exhibits slow westward propagation. Based on the tilt of the $r = 0.4$ contour, the propagation speed is roughly −1.8° day^{-1} (about −2.1 m s^{-1} at 24.75°N). Similarly, r for the 700-hPa height at 20.25°N (Fig. 4b) also exhibits slow westward propagation at a similar speed. The blue contours in Fig. 4b, which are copied from Fig. 4a, show the longitude and lag relationship between the lower- and upper-level circulations. At 700 hPa, the contours of $r = -0.5$ and −0.6 first appear inside the region

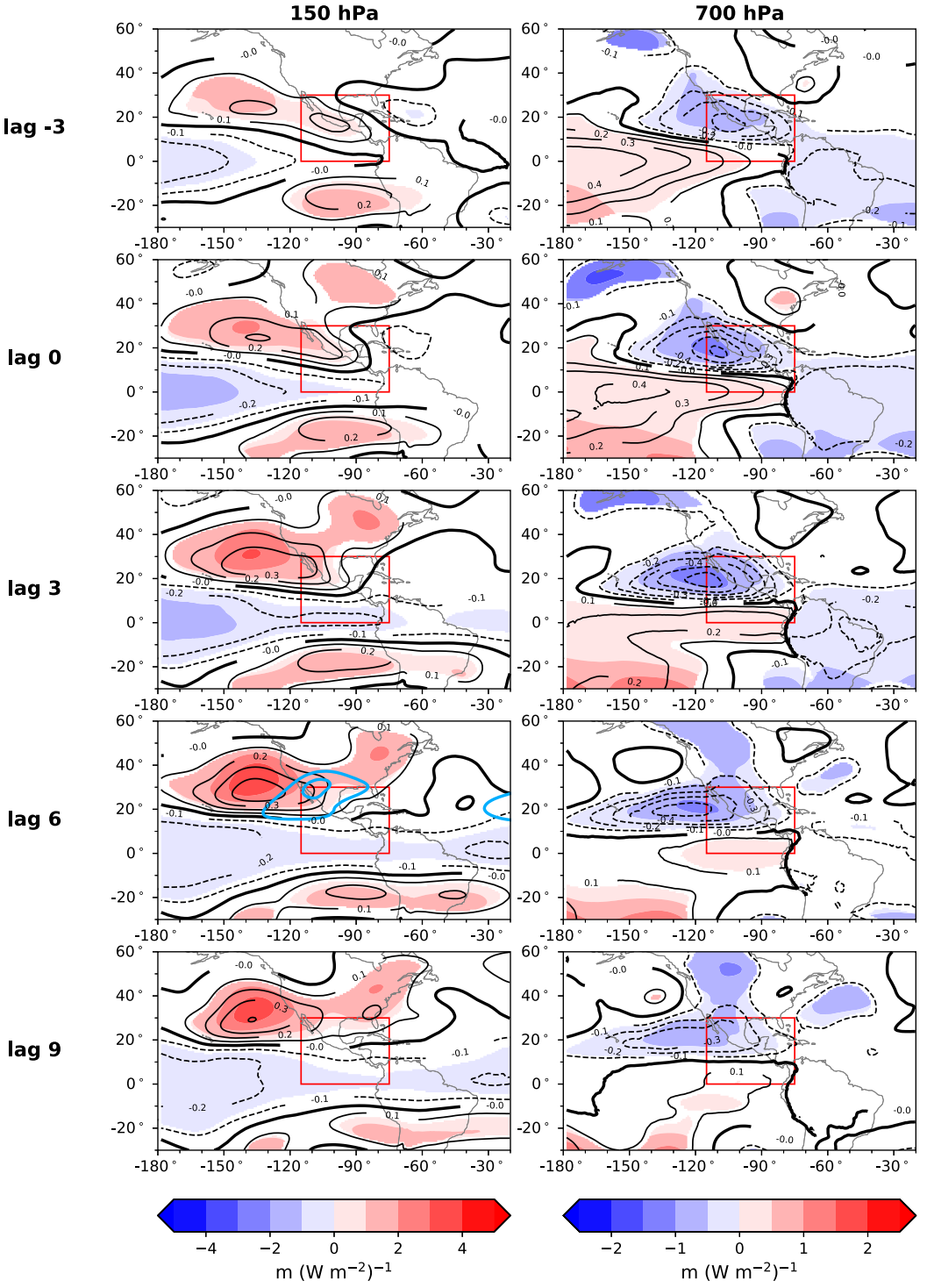

FIG. 2. Correlation coefficient r (black contours; interval: 0.1, dashed negative) and slope m (filled contours) between pentad-mean time series of geopotential height at each ERA5 grid point and −OLR averaged inside the red box. Filled contours are plotted where the confidence level of r is at or above the 99% level. Each row represents a distinct lag in days, where a positive lag means that OLR precedes geopotential height. The columns show geopotential height at (left) 150 and (right) 700 hPa. Contour intervals of m are 1 and 0.5 m (W m^{-2})$^{-1}$ for the left and right columns, respectively. In the 150-hPa lag-6 panel, thick blue contours are the 14 225- and 14 250-m contours of 1979–2019 mean geopotential height.

TABLE 1. Standard deviation of pentad-mean and July–August-mean OLR and precipitation rate time series for each region (A–C and A + B + C).

	Pentad time series				Jul–Aug time series			
	A + B + C	A	B	C	A + B + C	A	B	C
OLR (W m^{-2})	7.01	8.59	11.49	8.96	2.91	3.16	4.29	5.30
P_{CAL} (mm day^{-1})	1.31	1.54	3.09	1.96	0.56	0.51	1.21	1.15

where OLR is averaged (delineated by the red vertical lines), suggesting that the lower-level anomalies are a local response to the heating. This is consistent with Hoskins and Karoly (1981) who studied the linear response to subtropical forcing in a five-layer baroclinic model and found that the low-level response is mostly confined to the source region. In contrast, the strong upper-tropospheric anomaly is mostly outside the source region, and its correlation maximizes after the lower-tropospheric correlations decay.

Popovic and Plumb (2002) found that the westward shedding of anticyclonic vortices associated with the Asian monsoon anticyclone propagates at roughly −7 to −8 m s^{-1} (estimated based on their Fig. 4). These speeds are much faster than what we found in our Fig. 4, so it is unlikely that the tracked feature is westward eddy shedding. Garny and Randel (2013) correlated the upper-level divergence averaged over 70°–110°E to the area of low potential vorticity, and showed in their Fig. 8 that the maximum correlation moved from roughly 75°–30°E over 4 days, corresponding to about −13 m s^{-1}. They stated that possible contributors to this westward propagation may be related to advection by the easterly winds of the anticyclone or to westward eddy shedding.

In the shallow-water model of Heckley and Gill (1984), the Rossby gyres forced by heating propagate westward as the model reaches steady state. In their simulations using asymmetric heating (cf. their Fig. 4), the wavefront propagated westward at a speed of about −8° day^{-1} (−9.3 m s^{-1}). This is much faster than the speed in our Fig. 4, so the westward propagation in our Fig. 4 is unlikely to represent a Rossby wave phase speed. However, the propagation speeds of the cyclonic and anticyclonic centers in Fig. 4 of Heckley and Gill (1984) are approximately −1.7° day^{-1} (estimated graphically using length scale $L = 10°$ and time scale $T = 1/4$ day). This is close to the observed longitudinal propagation speed (−1.8° day^{-1}) of the correlation maximum in our Fig. 4.

A similar correlation analysis is applied to ERA5 temperatures, and the resulting r and m are shown in Fig. 5. Note that the selected pressure levels are different from those in Fig. 2. Here we find notable correlations in the same region where anticyclonic anomalies are found at 150 hPa, with r at 100 hPa negative and r at 300 hPa positive, depicting a cold anomaly above and warm anomaly below the anticyclonic anomaly. The magnitude of the temperature anomalies can be calculated from m; at lag +6, m values in the core of the cold and warm anomalies are around −0.15 and 0.10 K (W m^{-2})$^{-1}$, respectively. Since the standard deviation of the OLR time series is 7.01 W m^{-2}, the corresponding cold and warm temperature anomalies are about −1.0 and 0.7 K (obtained by multiplying m by the standard deviation), respectively.

Longitude–pressure cross sections of r taken at 24.75° and 20.25°N (Fig. 6) show that the height anomalies exhibit a first tropospheric internal mode (Hoskins and Jin 1991) structure, and also demonstrate the quadrature relationship between temperature and geopotential height. At both latitudes, the strongest anticyclonic anomaly is near 150 hPa. Cold and warm temperature anomalies are located above and below the anticyclonic anomaly, respectively. The positive r contours of the anticyclonic anomaly at 24.75°N overlaps with the region of northward meridional wind, showing that this anomaly is in the western sector of the climatological anticyclone. The region of negative correlations for geopotential height is seen at and below 400 hPa. At 24.75°N, r exceeds 0.4 in the regions

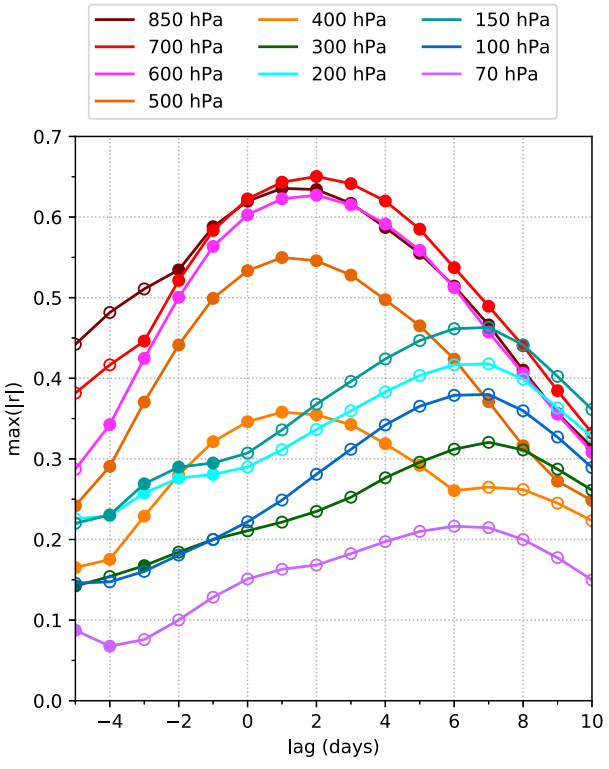

FIG. 3. Maximum of |r| in 0°–60°N, 180°W–0°, as a function of lag. Values of r are computed using pentad-mean time series of ERA5 geopotential at each grid point and −OLR averaged over the red box in Fig. 2. The unfilled (filled) circle symbol indicates that the r value with the largest absolute value is positive (negative).

TABLE 2. Lags at which $|r|$ are largest in Fig. 3, their corresponding r values, and the longitude and latitude at which the maxima occur.

Level (hPa)	Lag (days)	r	Lon (°W)	Lat (°N)
70	6	0.215	141.75	36.00
100	7	0.377	138.00	30.00
150	7	0.461	136.50	28.50
200	7	0.417	135.75	28.50
300	7	0.321	137.25	30.00
400	1	−0.359	110.25	16.50
500	1	−0.552	111.00	18.00
600	2	−0.629	112.50	18.75
700	2	−0.652	112.50	18.75
850	1	−0.637	112.50	18.75

corresponding to positive (negative) height anomalies in the upper (lower) troposphere. At 20.25°N, $r > 0.6$ is observed at 600–850 hPa, but the upper-tropospheric height anomaly is weaker. The vertical structure observed here is consistent with DeMaria (1985) (cf. his Figs. 6 and 10), who examined the three-dimensional structure of the atmospheric response to tropical heating. The structure in our Fig. 6a exhibits westward tilt, while Fig. 6b does not. In the results of DeMaria (1985), there is a slight westward tilt in the temperature anomalies (his Fig. 6a) but not in the height anomalies.

The anticyclonic anomaly appears to be deeper at 24.75°N than at 20.25°N, since the $r = 0.1$ contour spans 70–300 hPa at the former latitude while the latter spans roughly 100–300 hPa. This difference in vertical extent can be at least partly explained by the Prandtl–Rossby–Burger relationship (Hoskins et al. 1985; Kiladis 1998) $H = fL/N$ where H is the vertical penetration depth of a potential vorticity (PV) anomaly, f is the Coriolis parameter, L is the length scale of the anomaly, and N is the Brunt–Väisälä frequency. Based on this relation, the PV anomaly at a higher latitude will have a larger vertical depth of influence.

The temperature anomalies reflects the thermal wind balance due to the vertical wind shear above and below the level of the anticyclonic core. The vertical wind shear above and below the core have opposing signs; below the core, the anticyclonic flow strengthens with increasing height, while the opposite is true above the core. The thermal wind relation is

$$\frac{\partial \mathbf{v}_g}{\partial z} = \frac{R}{Hf}\hat{\mathbf{k}} \times \nabla_z T, \tag{2}$$

where $\mathbf{v}_g = (u_g, v_g)$ is the geostrophic wind, z is the log–pressure height, R is the gas constant for dry air, H is the scale height, f is the Coriolis parameter, and T is temperature. It can be inferred that above (below) the core, the sign of the shear requires that $\nabla_z T$ points outward from (inward to) the center of the anomaly, implying that the surrounding air is warmer (cooler) than in the center. The cold (warm) anomaly above (below) the core is consistent with this. Alternatively, the thermal anomalies can be understood by evaluating the curl of Eq. (2) and taking the vertical component, from which one finds $\partial_z \xi_g \propto \nabla_z^2 T$ where $\xi_g = \hat{\mathbf{k}} \cdot \nabla \times \mathbf{v}_g$ is the geostrophic relative vorticity. Below the anticyclonic core, $\partial_z \xi_g < 0$ and hence $\nabla_z^2 T < 0$, indicating that the surrounding temperature is lower, and vice versa. As Sardeshmukh and Hoskins (1988) stated, vertical ascent above

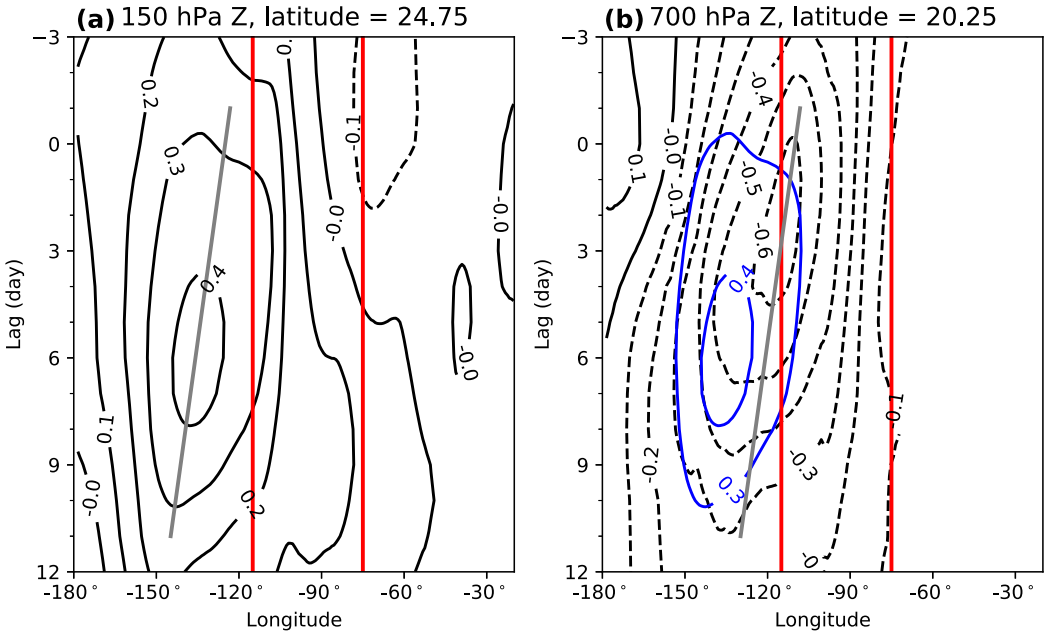

FIG. 4. Longitude–lag plot of r for (a) 150-hPa geopotential height at 24.75°N and (b) 700-hPa geopotential height at 20.25°N. Contours of r (black) have intervals of 0.1 and dashed contours indicate negative values. Blue contours in (b) are the $r = 0.3$ and $r = 0.4$ contours from (a). Red vertical lines indicate the western (115°W) and eastern (75°W) boundary of the region used for averaging OLR. Gray lines denote the $-1.8°$ day^{-1} slope.

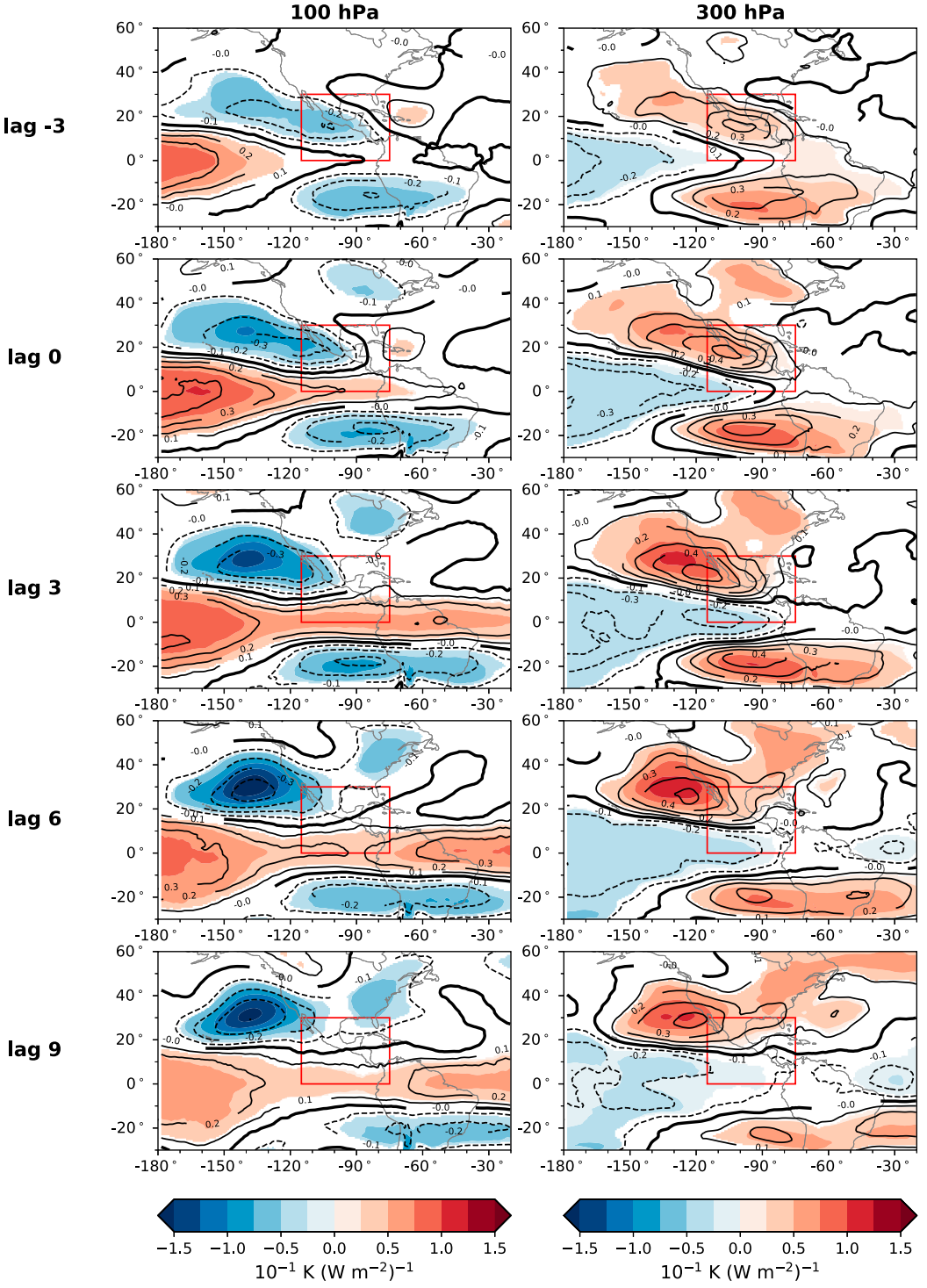

FIG. 5. As in Fig. 2, but for ERA5 temperature at (left) 100 and (right) 300 hPa.

the core (adiabatic cooling) and descent below (adiabatic heating) would be set up in order to maintain this balance.

OLR is closely related to precipitation but is not a direct measure of it. We use IMERG precipitation retrievals in a similar lagged correlation analysis by computing pentad-mean time series that represent the average precipitation rate inside the combined region of A, B, and C in Fig. 1. While the OLR time series span 1979–2019, the IMERG time series is shorter (2000–19). IMERG provides multiple types of precipitation retrievals, and here we use the *precipitationCal* data (P_{CAL}),

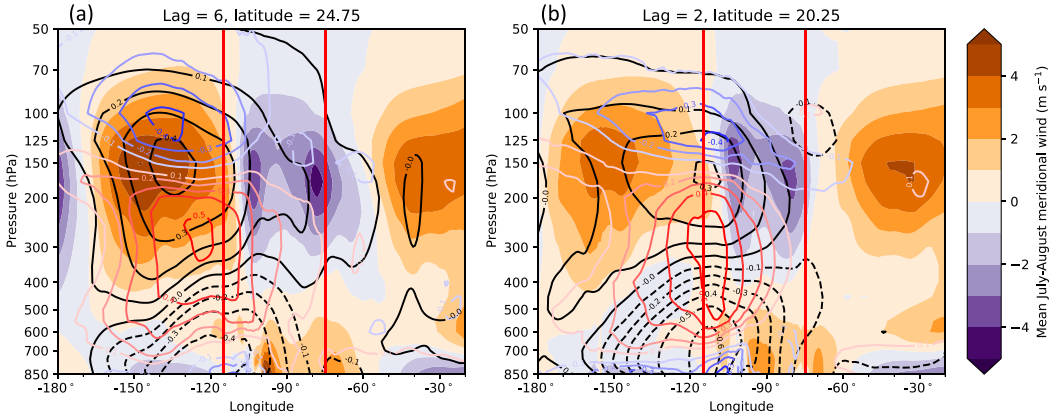

FIG. 6. (a) Longitude–pressure section of lag +6 *r* between pentad-mean −OLR and geopotential height (black contours; interval: 0.1, dashed negative), and −OLR and temperature (unfilled colored contours; interval: 0.1, blue negative) at 24.75°N. Vertical red lines indicate the western and eastern boundaries of the OLR box shown in Figs. 2 and 5. Filled contours represent the July–August (1979–2019) mean meridional wind at intervals of 1 m s^{-1}. (b) As in (a), but for lag +2 and 20.25°N.

which represents multisatellite precipitation retrievals with gauge calibration. Values of *r* and *m* from lagged correlations obtained using P_{CAL} are shown in Fig. 7.

Values of *r* and *m* for P_{CAL} closely resemble Figs. 2 and 5 when comparing the same lag and height. The magnitude, size, and location of the anticyclonic/cyclonic anomalies are all similar. Based on the *m* and the standard deviation of the P_{CAL} given in Table 1, it is inferred that for a forcing magnitude of one standard deviation of P_{CAL}, the height anomaly at 150 hPa is ~31 m and the temperature anomaly at 100 hPa is ~−1 K. Both are comparable to the results derived from OLR. The vertical cross section of *r* at 24.75°N derived from P_{CAL} (not shown) also closely resembles Fig. 6. Based on these results it can be concluded that this analysis depicts the presence of anticyclonic, cyclonic, and temperature anomalies using either OLR or precipitation data.

Our results can be compared to those of Stensrud (2013), who studied the influence of deep convection associated with the NAM on the large-scale circulation over North America through a case study using the WRF model. In a 6-day simulation, he showed that monsoon convection is associated with the formation of an anticyclonic anomaly at 200 hPa over western Mexico during days 1–3, and in days 4–6 this anomaly expands westward into the eastern Pacific Ocean (cf. his Fig. 7). The forced anticyclone in his simulation spans 20°–35°N, comparable to the anomalies seen in our Fig. 2 at 150 hPa. The westward extent of the anomalies are also similar between his and our study; at day 6 of his simulation, the anticyclonic anomaly has propagated westward to approximately 145°W, while the anomaly we found at day 6 extends westward to 150°W. His results also demonstrate the cold (warm) temperature anomalies above (below) the forced anticyclones. The speed of westward propagation in the model is about −7 m s^{-1} in Stensrud (2013) (~6° day^{-1}), however, compared to the −1.8° day^{-1} we observe in Fig. 4.

Stensrud (2013) also found a cyclonic anomaly at 700 hPa at day 6, though it was mostly situated over western Mexico (collocated with the area of convection). This is unlike the

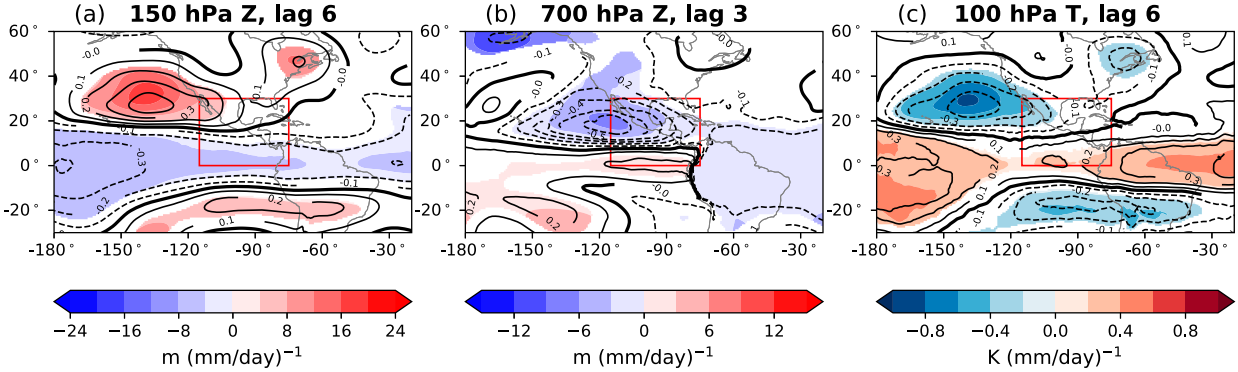

FIG. 7. Correlation coefficient *r* (black contours; interval: 0.1, dashed negative) and slope *m* (filled contours) from correlations using IMERG P_{CAL}. (a) The *r* and *m* for 150-hPa geopotential height at lag +6, (b) 700-hPa geopotential height at lag +3, and (c) 100-hPa temperature at lag +6. Colored regions are where the statistical confidence of *r* is at or above 99%.

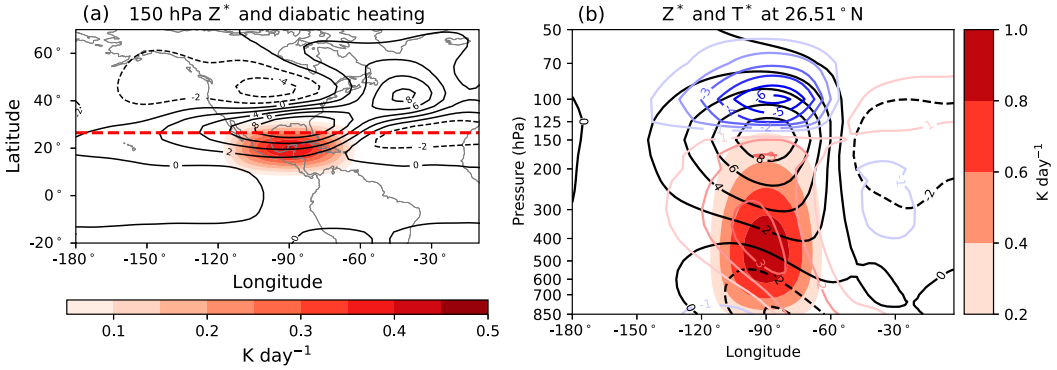

FIG. 8. (a) Zonally asymmetric component of geopotential height Z^* (black contours; interval: 2 dam, dashed negative) and thermal forcing (filled contours) at 150 hPa. (b) Vertical cross section of Z^* (black contours; interval: 2 dam), T^* (unfilled blue and red contours; interval: 1 K, blue negative), and diabatic heating (filled contours) at 26.5°N [red dashed line in (a)].

feature in our Fig. 2, which extends into the Pacific. His case study covers the time period from 1200 UTC 28 June to 1200 UTC 4 July 2006, while our study period covers mid-June to mid-September over multiple years. Variations of the basic flow during different time periods may have contributed to the differences in our results.

In Figs. 2 and 7, slope maxima indicating positive height anomalies are observed at around 45°N, 85°W at 150 hPa. The r corresponding to this anomaly is slightly higher when using IMERG (Fig. 7) compared to that of OLR (Fig. 2). At a similar location (45°N, 75°W) the experiments by Stensrud (2013) also exhibit a positive height anomaly, which he interprets as the downstream propagation of Rossby wave trains emanating from the NAM region. We find that although r is small in this region (<0.2), it is statistically significant; and the wave propagation described by Stensrud (2013) may explain the presence of the local correlation in this region.

b. *Comparison to simplified GCM runs*

Here we compare the results of section 3a to those of Siu and Bowman (2019), who used a simplified dry general circulation model (GCM) to examine the atmospheric response to various thermal forcing configurations. The model utilizes the spectral dynamical core of the NCAR Community Atmosphere Model and a Held–Suarez-like idealized physics package (Held and Suarez 1994), with modifications according to Schneider (2004) and Schneider and Walker (2006) that produce a better tropical circulation. The reader is referred to Siu and Bowman (2019) for details regarding the model parameters and configuration.

Siu and Bowman (2019) demonstrated that this model is able to reproduce a realistic boreal summer UTLS circulation when using a diabatic heating distribution based on TRMM satellite data [Run 2a of Siu and Bowman (2019, their Fig. 4b)]. Both the AMA and NAMA are present in that run. To focus on the NAMA, in this study we analyze Run 5e of Siu and Bowman (2019), which is forced by an idealized steady heating distribution centered at 20°N, as shown in Figs. 8a and 8b. The heating is distributed vertically between 100 and 1000 hPa with a peak at near 450 hPa. This run is selected because the latitudinal and longitudinal extent of its imposed heating is similar to the OLR box used in section 3a.

The zonally asymmetric part of the geopotential height Z^* is calculated as $Z^* = Z - [Z]$, where Z is the geopotential height and the square brackets denote the zonal mean. The total time integration in this experiment is 600 days, and the average Z^* at 150 hPa from the last 300 days of the run is shown in Fig. 8a. An anticyclonic anomaly is found north of the forcing. The zonally asymmetric part of the temperature T^* is calculated in the same way, and the vertical structure of Z^* and T^* at 26.5°N are shown in Fig. 8b. The upper-tropospheric Z^* is positive and maximizes near the 150-hPa level, and negative (positive) T^* are found above (below). Such a vertical configuration agrees well with the observational results in Fig. 6, which supports the idea that the lagged correlations show the structure of the forced atmospheric response to diabatic heating. Although the location of the specified diabatic heating in the numerical experiment is similar to the box used to average the observed OLR and precipitation, the simulated anticyclone is located east of what is seen in observations. The model also has less westward tilt in the response than is observed. Siu and Bowman (2019) noted similar eastward displacements in the idealized model when using realistic geographic heating distributions. These may be a result of errors in the strength of the subtropical jet in the model due to the limitations of the idealized forcing.

c. *Sensitivity of results to OLR averaging domain*

Hu and Tung (2002) suggest that, in the NAM, the precipitation regime over the northwestern Mexico and southwestern U.S. region is different than that over southern-central Mexico, and that they have a tendency to oppose each other. Aside from the NAM, the ITCZ is also a significant source of precipitation and latent heat release. In this section we separately examine the effects of each region on the large-scale circulation. The domain for averaging OLR used in the previous section is split into three regions by latitude as shown in Fig. 1; regions A, B, and C cover 20°–30°, 10°–20°, and 0°–10°N, respectively. We construct separate OLR pentads for each of

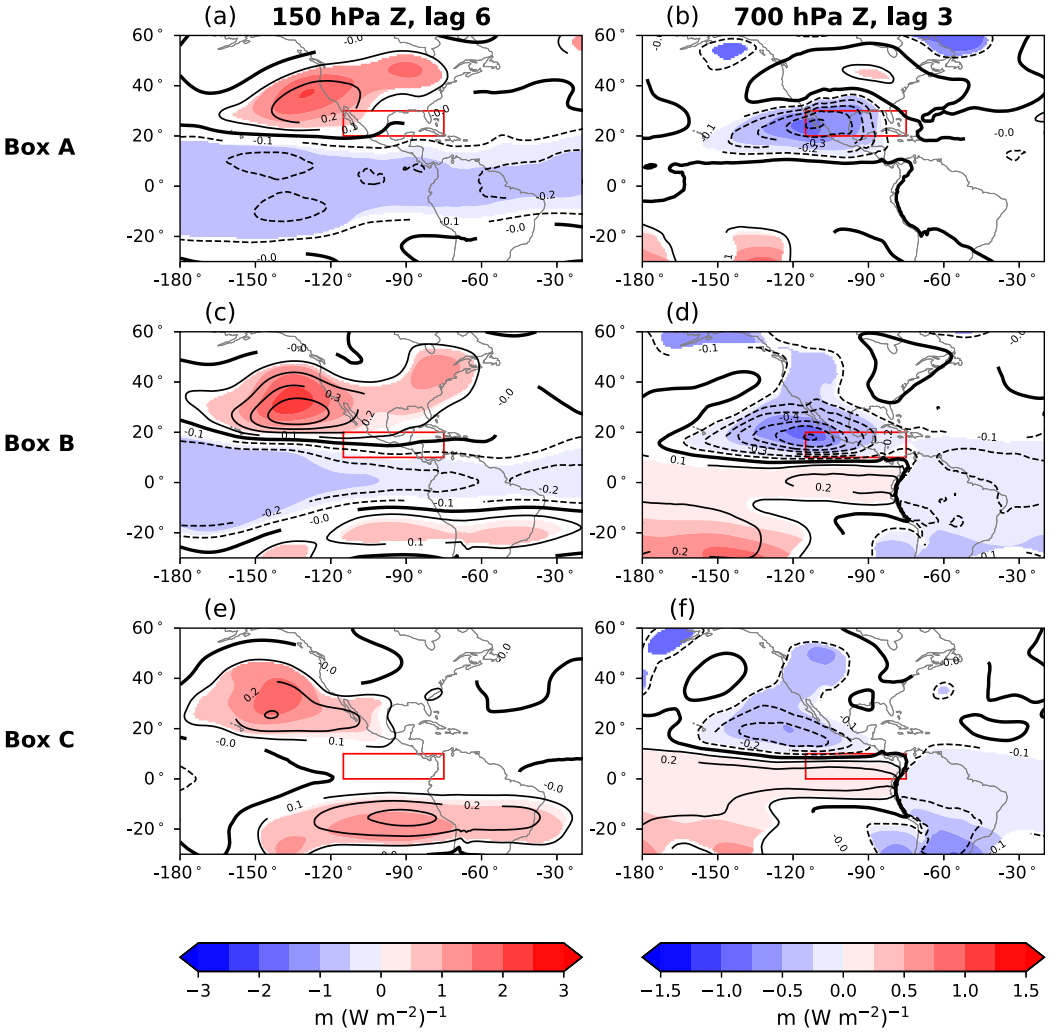

FIG. 9. Correlation coefficient r (black contours; interval: 0.1, dashed negative) and slope m (filled contours) using −OLR pentad time series averaged in (a),(b) region A; (c),(d) region B; and (e),(f) region C. Columns shows (left) 150-hPa geopotential height at lag +6 and (right) 700-hPa geopotential height at lag +3.

these boxes and perform the correlation analysis similar to section 3a.

The spatial distributions of r and m for geopotential height at 150 hPa (lag +6) and 700 hPa (lag +3) obtained from each of the three boxes are shown in Fig. 9. All three cases exhibit an anticyclonic anomaly to the west of the United States and Mexico, with region B having the largest values of r (>0.4). Siu and Bowman (2019) conducted numerical experiments where the heating distribution shown in Fig. 8a is centered on 0°, 5°, . . . , 20°N, and found that the anticyclonic responses tend to strengthen with increasing latitude. Here we find that region B has the strongest correlation with the anticyclonic anomaly. The July–August climatological mean precipitation rates for regions A, B, C, and A + B + C are 3.72, 7.69, 7.33, and 6.24 mm day^{-1}, respectively. The stronger correlation signal associated with region B may be attributable to the larger amount of precipitation in region B than in region A, although the latter is at a higher latitude where diabatic heating may be more potent in forcing the Gill-type response. The pattern of Fig. 9c closely resembles that of Fig. 2, suggesting that the precipitation in region B is the dominant forcing by a small amount. The correlation pattern at 700 hPa also depicts a similar tendency where region B exhibits the largest values of r. As the box shifts toward the equator (box C, Fig. 9e), r at 150 hPa in the Southern Hemisphere becomes stronger. This is to be expected, because heating sources close to the equator can force response patterns with a high degree of symmetry about the equator, even if the heating is located off of the equator (Sardeshmukh and Hoskins 1988; Dima et al. 2005).

Although region A contains the NAM precipitation from northwestern Mexico, it also includes the Gulf of Mexico and the Florida panhandle. Convection from both regions may contribute to the forcing of the NAMA. Correlations computed for the eastern and western halves of box A (not shown) show that each has comparable contribution to the NAMA. At 150 hPa, the eastern half has slightly weaker r and a response

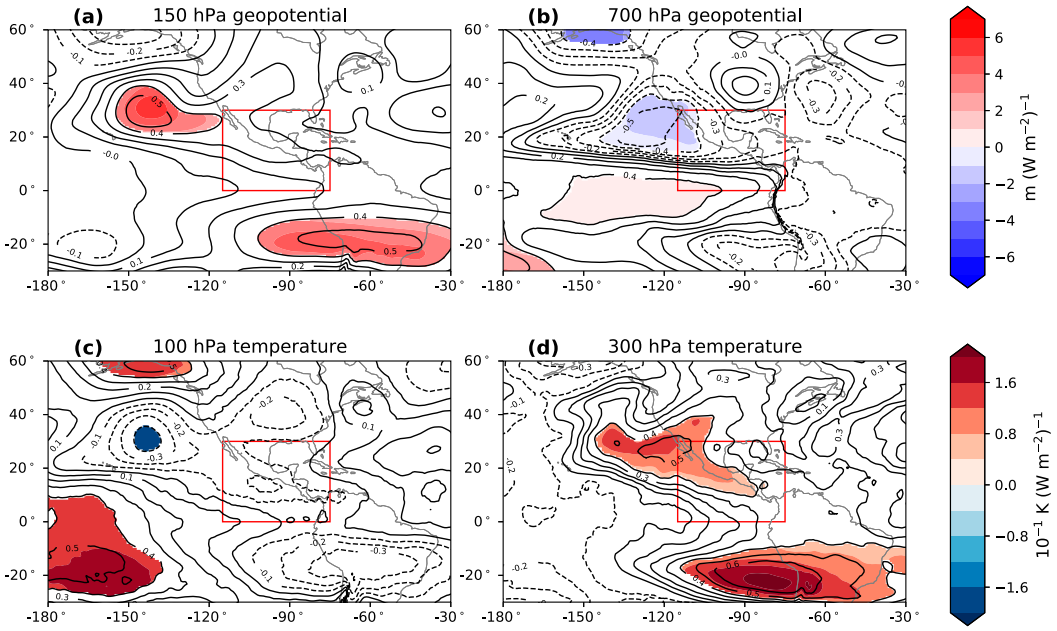

FIG. 10. The r (black contours; interval: 0.1, dashed negative) and m (filled contours) of July–August-mean time series (1979–2019) calculated using −OLR averaged in the red box and (a) 150-hPa geopotential height, (b) 700-hPa geopotential height, (c) 100-hPa temperature, and (d) 300-hPa temperature. Colored contours are plotted where the statistical confidence of r is at or above the 99% level.

that is shifted eastward compared that of the western half, but the results show that precipitation over both the southeastern United States and the Gulf of Mexico regions can contribute to the NAMA.

d. Correlations and composites at the interannual time scale

In this section we investigate variability at the interannual time scale by computing correlations of July–August monthly means for 1979–2019. As in section 3a, the time series of OLR represents the average inside the entire box (A + B + C). Time series are detrended before calculating correlations.

Figure 10 shows the spatial distributions of r and m for 150- and 700-hPa geopotential heights and 100- and 300-hPa temperatures. Statistical testing for r is done in the same way as in the pentad correlations: by evaluating the effective degrees of freedom using lag 1 autocorrelation and a two-tailed Student's t test. Similar to Fig. 2, r at 150-hPa geopotential height (Fig. 10a) has two regions of significant positive correlations: one centered near 30°N, 145°W and another near 20°S, 60°W. Both regions' r values exceed 0.5, which is higher than that of the pentad correlations. Aside from the difference in magnitude, the spatial distributions of r at interannual and intraseasonal time scales are quite similar. Likewise, the interannual correlation of 700-hPa geopotential height (Fig. 10b) is also similar to the pentad correlations, showing a cyclonic anomaly to the west of the OLR box. Although the magnitudes of r are comparable to those from intraseasonal correlations, the regions at 99% confidence are smaller in area due to the smaller sample size (41).

Figures 10c and 10d show r at 100 and 300 hPa for temperature. These also resemble the pentad correlations and are consistent with the temperature anomalies at the intraseasonal time scale. The cold anomalies at 100 hPa, however, have weaker correlations at the interannual time scale. The vertical cross section of r (Fig. 11) shares the main features with Fig. 6 such as the core of anticyclonic anomaly at ~150 hPa, the cold (warm) anomaly above (below) this level, and the cyclonic anomaly in the lower troposphere.

Correlations based on regions A, B, and C are shown in Fig. 12. Region B has the strongest correlations with geopotential height of the three, similar to the pentad correlations in Fig. 9, while region C exhibits strong correlations with the Southern Hemisphere at 150 hPa. At both intraseasonal and interannual time scales, precipitation in box B is most strongly correlated with circulation anomalies near the southern United States and northern Mexico. Like the pentad correlations, the anomaly per OLR standard deviation can be calculated using m and the values provided in Table 1. We find that the positive height anomaly associated with region B is ~15 m per OLR standard deviation.

Composites based on average July–August OLR are shown in Fig. 13. The mean geopotential height of the upper quartiles (10 years out of 41 years) of average OLR in each regions A–C are shown in the first column (Figs. 13a,d,g) while the lower quartiles are shown in the second column (Figs. 13b,e,h).Figures 13a,d,g have smaller contours at 1425 and 1422.5 dam, indicating a smaller climatological anticyclone. This is consistent with the idea that periods with less precipitation (higher OLR) provide less forcing for the NAMA. In contrast, Figs. 13b,e have larger anticyclones, indicating that the months with more precipitation are associated with a larger NAMA. The difference between the

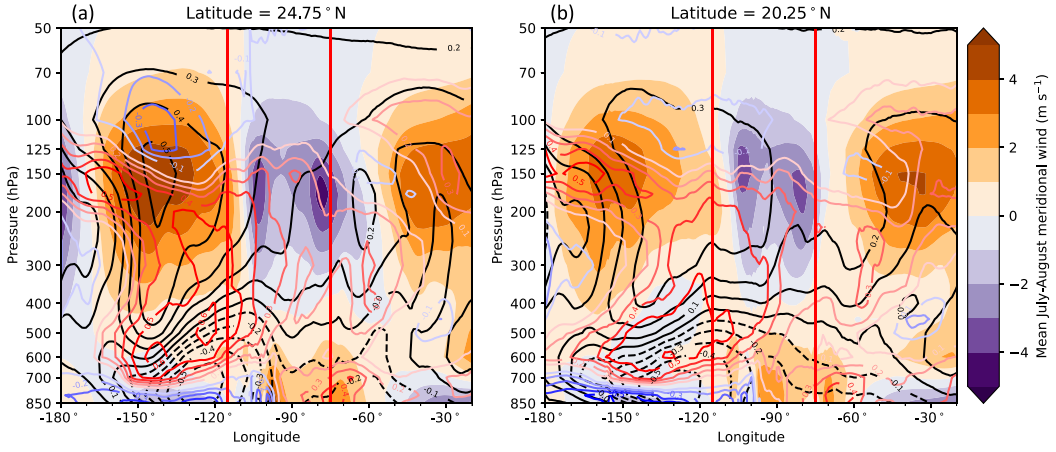

FIG. 11. (a) Longitude–pressure section of r at 24.75°N between July and August-mean −OLR and geopotential height (black contours; interval: 0.1, dashed negative), and between mean −OLR and temperature (blue and red contours; interval: 0.1, blue negative). Vertical red lines indicate the western and eastern boundaries of the OLR box in Fig. 10. Filled contours represent the July–August (1979–2019)-mean meridional wind at an interval of 1 m s^{-1}. (b) As in (a), but at 20.25°N.

lower and upper quartiles are shown in Figs. 13c,f,i, and the resulting morphologies of the anomalies are similar to those in Fig. 12. Region B exhibits the strongest anomalies inside 20°–40°N, while region A has strong anomalies north of 40°N and region C has strong anomalies near 20°S. The statistical testing in Figs. 13c,f,i are performed by the unequal variance t test. Due to the small sample size, we show the regions at or above 95% confidence. No anomalies are at the 99% confidence level. However, the composites are qualitatively consistent with all previous results.

Comparing Figs. 13d and 13e gives some insight into why the strongest positive height anomalies are found west of the NAMA core in both the intraseasonal and interannual correlations. During summers of low OLR, the NAMA is larger and extends farther westward and eastward. However, the geopotential height in the core of the NAMA is not significantly higher. As a result, the anomalies shown in Fig. 13f are most apparent on the west and east flanks of the NAMA, with the western side having stronger anomalies. Though weak, the eastern anomaly is also apparent in the correlation analyses (e.g., Figs. 7a, 9c, 12c). The similarity between the interannual correlations/composites and the intraseasonal correlations suggests that the forced response to regional diabatic heating is similar across these time scales.

4. Summary and discussion

ERA5 and OLR data from 1979 to 2019 are used to assess the variability of the circulation and temperature and their connection to precipitation in the low-latitude North American and Central American region. We find that precipitation in this region is associated with an anticyclonic anomaly west of Baja California that tends to be strongest near 150 hPa, with a lag of ~7 days with respect to the OLR or precipitation. There is also a cyclonic anomaly below 600 hPa that maximizes with a lag of 1–2 days with respect to OLR. The structure agrees well with theory derived from the two-layer model (Matsuno 1966; Gill 1980) and also a stratified model (DeMaria 1985). In section 3b we demonstrate that the vertical structure of geopotential and temperature anomalies found in correlations using pentad time series agrees well with the structure of atmospheric response to diabatic heating simulated by an idealized dry GCM (Siu and Bowman 2019).

Our results share some similarity with those of Randel and Park (2006), who investigated the connection between convection associated with the Asian monsoon and its UTLS anticyclone. Similar to our approach, they use a time series of area-averaged OLR as a proxy for deep convection. Low OLR is shown to correlate to the area of low PV, with the strongest correlations near a lag of 5 days (deep convection precedes low PV). This is similar to our finding that the largest correlations occur at lags of 7 days. Randel and Park (2006) also correlate the OLR time series to temperature (their Fig. 6), resulting in a vertical temperature dipole similar to our Fig. 6. At 300 hPa, they find that the strongest OLR–temperature correlation occurs northwest of the convective region (their Fig. 6b), which resembles the warm temperature anomaly shown in our Fig. 5. Based on these similarities, we infer that the convection–UTLS connection in the NAM and Asian monsoon have similar characteristics.

The role of rainfall at different latitudes is investigated by performing correlation analyses for the subregions A, B, and C in Fig. 1. Region B exhibits the strongest correlations between OLR or precipitation and circulation anomalies in the UTLS and lower troposphere, and the pattern and magnitudes of the correlation with region B are most similar to those for the entire region. One likely explanation for the strong signal from region B is that the relatively more abundant rainfall in region B relative to A and its higher latitude relative to C make the

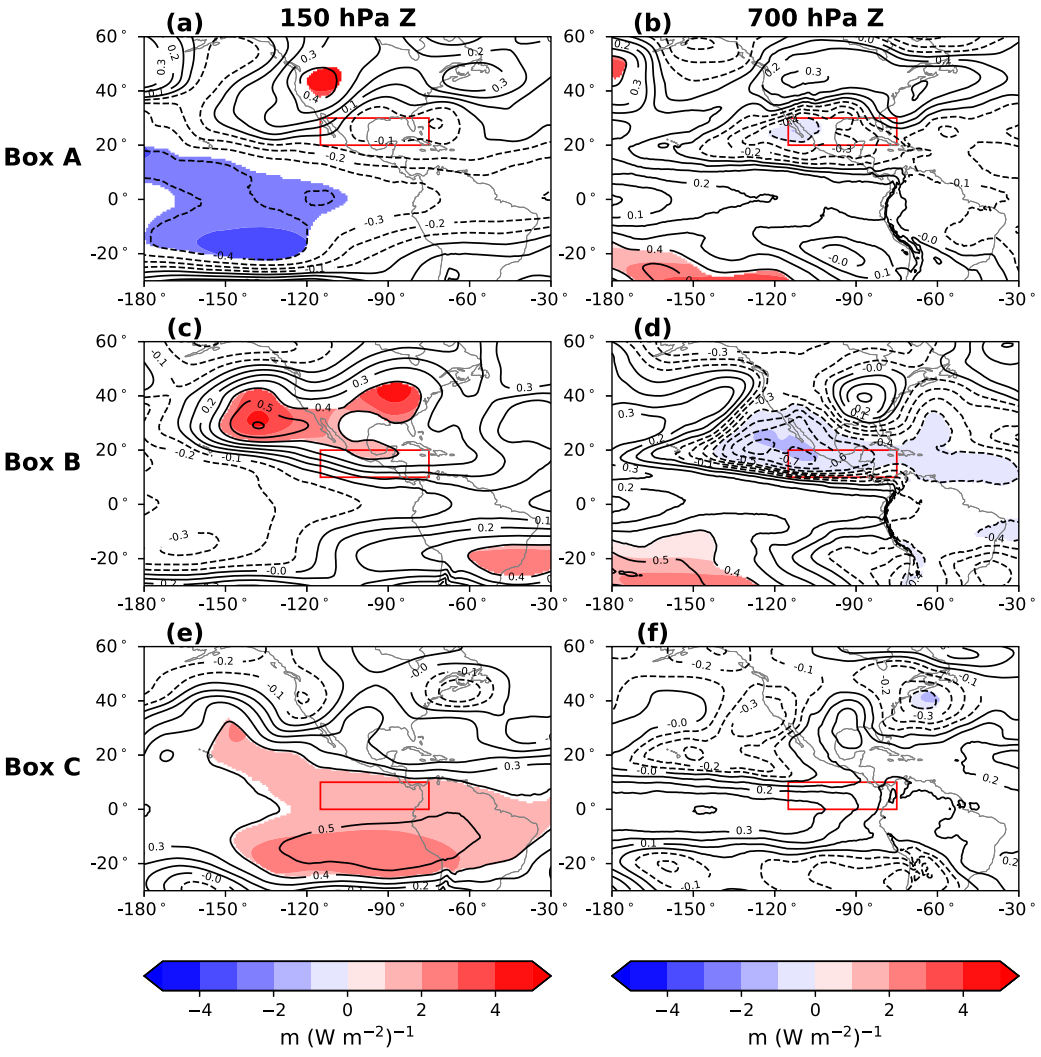

FIG. 12. The r (black contours; interval: 0.1, dashed negative) and m (filled contours) using July–August-mean −OLR averaged in (a),(b) region A; (c),(d) region B; and (e),(f) region C at (a),(c),(e) 150- and (b),(d),(f) 700-hPa geopotential heights.

diabatic heating in region B more effective in influencing the large-scale circulation.

Correlations using July–August monthly mean time series show that the horizontal and vertical correlation patterns resemble those derived from pentad time series, suggesting that the relationship at interannual time scales are similar to those at the intraseasonal time scale. Composites of mean geopotential height based on the upper or lower quartile of July–August mean OLR provides some insight as to why the positive height anomalies are found to be west of the NAMA core. During periods of low OLR in region B, the NAMA expands both eastward and westward. In contrast, the height in the core of the NAMA does not vary much with OLR. This results in anomalies on the western and eastern flanks of the NAMA, with the western side having the stronger height anomalies. The explanation for why the strong anticyclonic anomalies are west of the U.S. coast in both the intraseasonal and interannual correlation analyses is that the longitudinal extent of the NAMA expands following periods of strong precipitation. In both the interannual correlation and composite analyses, we find that region B is most strongly associated with anomalies linked to the NAMA.

Aside from the horizontal distribution of rainfall, the vertical distribution of diabatic heating may also influence the magnitude and pattern of the forced response. Since OLR and IMERG are related to total precipitation and in turn the vertically integrated heating, this study does not account for vertical variations of heating. Siu and Bowman (2019) found that the response is sensitive to the shape of the heating profile and used a slightly top-heavy heating profile for their simulations. Jin and Hoskins (1995) noted that the low-level response is significantly stronger when the imposed heating peak is lower. Schumacher et al. (2004) and Chang and L'Ecuyer (2019) found that the atmospheric response is sensitive to the vertical

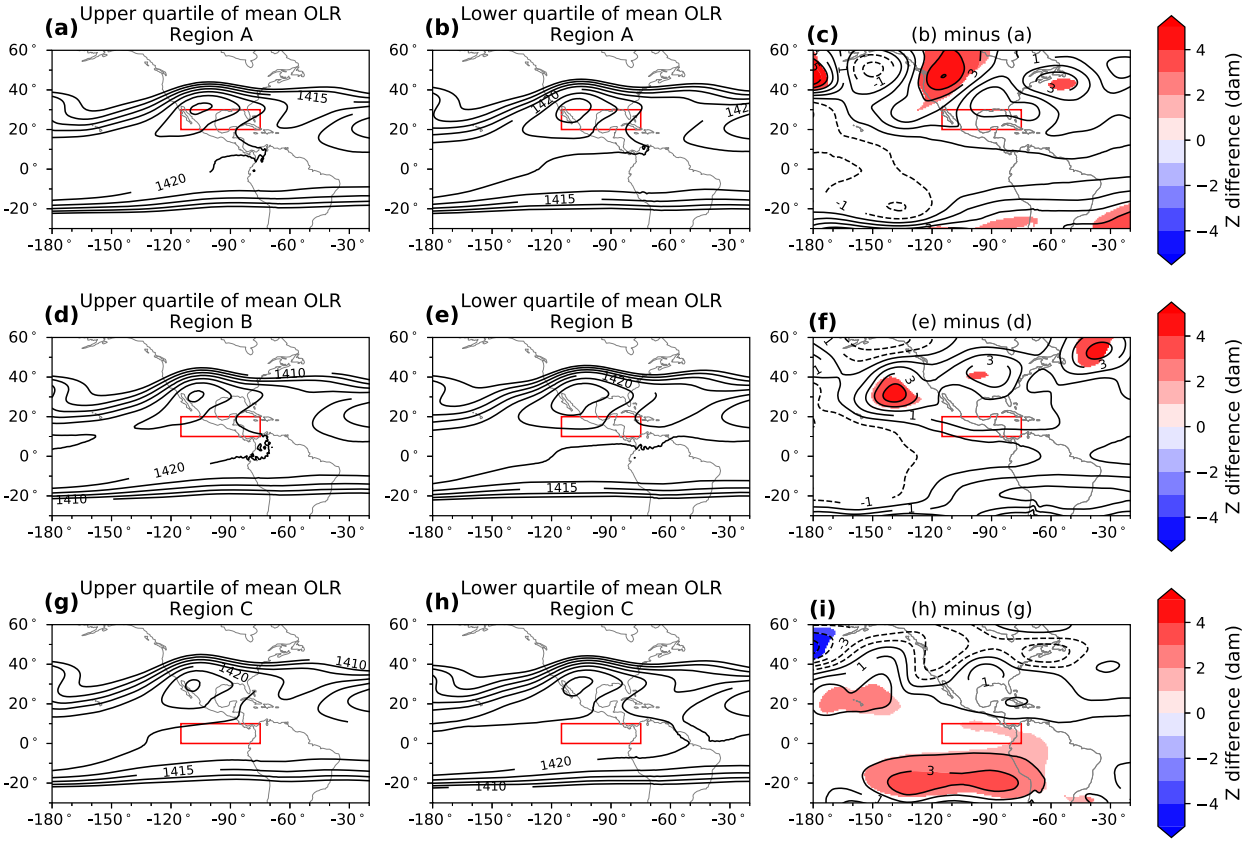

FIG. 13. Mean July–August 150-hPa geopotential height composited on the upper quartile of mean OLR in region (a) A, (d) B, and (g) C. (b),(e),(h) Composite means of the lower quartiles. (c),(f),(i) The differences between the mean of the lower quartile and of the upper quartile. Colored regions are where the confidence is at or above the 95% level. Contour intervals are 1 dam for (c), (f), and (i), and 2.5 dam for all other plots. Colored contours in (c), (f), and (i) have identical intervals as the black contours.

profile of latent heating, and both studies suggest that increased stratiform rain, which is characterized by top-heavy heating, would increase the strength of the upper-level response. It is possible that the variability of the NAMA is connected to vertical variations of latent heating and the partitioning between convective and stratiform rainfall.

Though we have demonstrated the connection between precipitation and an anticyclonic circulation anomaly in the UTLS, the magnitude of correlation coefficients at 150 hPa ($0.4 < r < 0.5$) suggests that a large portion of variance in the upper-tropospheric flow is related to other factors. These could include Rossby waves propagating along the subtropical jet and internal dynamics of the anticyclonic flow.

Acknowledgments. This work is funded by the National Aeronautics and Space Administration Grant 80NSSC19K0341 to Texas A&M University. LWS is partly supported by the National Science Foundation through Grant AGS-1840979 to Cornell University. We thank two anonymous reviewers whose comments have significantly improved this manuscript.

Data availability statement. ERA5 data are available from the Copernicus Climate Data Store (https://cds.climate.copernicus.eu). The NOAA Interpolated OLR data are provided by the NOAA/OAR/ESRL PSL (https://psl.noaa.gov/). IMERG products can be obtained from NASA's Goddard Earth Sciences Data and Information Services Center (GES DISC) (https://disc.gsfc.nasa.gov/).

REFERENCES

Adams, D. K., and A. C. Comrie, 1997: The North American monsoon. *Bull. Amer. Meteor. Soc.*, **78**, 2197–2213, https://doi.org/10.1175/1520-0477(1997)078<2197:TNAM>2.0.CO;2.

Barlow, M., S. Nigam, and E. H. Berbery, 1998: Evolution of the North American monsoon system. *J. Climate*, **11**, 2238–2257, https://doi.org/10.1175/1520-0442(1998)011<2238:EOTNAM>2.0.CO;2.

Bretherton, C. S., M. Widmann, V. P. Dymnikov, J. M. Wallace, and I. Bladé, 1999: The effective number of spatial degrees of freedom of a time-varying field. *J. Climate*, **12**, 1990–2009, https://doi.org/10.1175/1520-0442(1999)012<1990:TENOSD>2.0.CO;2.

Chang, K.-W., and T. S. L'Ecuyer, 2019: Role of latent heating vertical distribution in the formation of the tropical cold trap. *J. Geophys. Res. Atmos.*, **124**, 7836–7851, https://doi.org/10.1029/2018JD030194.

Clapp, C. E., J. B. Smith, K. M. Bedka, and J. G. Anderson, 2019: Identifying source regions and the distribution of cross-tropopause convective outflow over North America during

the warm season. *J. Geophys. Res. Atmos.*, **124**, 13750–13762, https://doi.org/10.1029/2019JD031382.

DeMaria, M., 1985: Linear response of a stratified tropical atmosphere to convective forcing. *J. Atmos. Sci.*, **42**, 1944–1959, https://doi.org/10.1175/1520-0469(1985)042<1944:LROAST>2.0.CO;2.

Dethof, A., A. O'Neill, J. M. Slingo, and H. G. Smit, 1999: A mechanism for moistening the lower stratosphere involving the Asian summer monsoon. *Quart. J. Roy. Meteor. Soc.*, **125**, 1079–1106, https://doi.org/10.1002/qj.1999.49712555602.

Diem, J. E., and D. P. Brown, 2009: Relationships among monsoon-season circulation patterns, gulf surges, and rainfall within the Lower Colorado River Basin, USA. *Theor. Appl. Climatol.*, **97**, 373–383, https://doi.org/10.1007/s00704-008-0081-x.

——, ——, and J. Mccann, 2013: Multi-decadal changes in the North American monsoon anticyclone. *Int. J. Climatol.*, **33**, 2274–2279, https://doi.org/10.1002/joc.3576.

Dima, I. M., J. M. Wallace, and I. Kraucunas, 2005: Tropical zonal momentum balance in the NCEP reanalyses. *J. Atmos. Sci.*, **62**, 2499–2513, https://doi.org/10.1175/JAS3486.1.

Douglas, M. W., R. A. Maddox, K. Howard, and S. Reyes, 1993: The Mexican monsoon. *J. Climate*, **6**, 1665–1677, https://doi.org/10.1175/1520-0442(1993)006<1665:TMM>2.0.CO;2.

Dunkerton, T. J., 1995: Evidence of meridional motion in the summer lower stratosphere adjacent to monsoon regions. *J. Geophys. Res.*, **100**, 16 675–16 688, https://doi.org/10.1029/95JD01263.

Garny, H., and W. J. Randel, 2013: Dynamic variability of the Asian monsoon anticyclone observed in potential vorticity and correlations with tracer distributions. *J. Geophys. Res. Atmos.*, **118**, 13 421–13 433, https://doi.org/10.1002/2013JD020908.

——, and ——, 2016: Transport pathways from the Asian monsoon anticyclone to the stratosphere. *Atmos. Chem. Phys.*, **16**, 2703–2718, https://doi.org/10.5194/acp-16-2703-2016.

Gettelman, A., D. E. Kinnison, T. J. Dunkerton, and G. P. Brasseur, 2004: Impact of monsoon circulations on the upper troposphere and lower stratosphere. *J. Geophys. Res.*, **109**, D22101, https://doi.org/10.1029/2004JD004878.

Gill, A. E., 1980: Some simple solutions for heat induced tropical circulation. *Quart. J. Roy. Meteor. Soc.*, **106**, 447–462, https://doi.org/10.1002/qj.49710644905.

Heckley, W. A., and A. E. Gill, 1984: Some simple analytical solutions to the problem of forced equatorial long waves. *Quart. J. Roy. Meteor. Soc.*, **110**, 203–217, https://doi.org/10.1002/qj.49711046314.

Held, I. M., and M. J. Suarez, 1994: A proposal for the intercomparison of the dynamical cores of atmospheric general circulation models. *Bull. Amer. Meteor. Soc.*, **75**, 1825–1830, https://doi.org/10.1175/1520-0477(1994)075<1825:APFTIO>2.0.CO;2.

Hersbach, H., and Coauthors, 2020: The ERA5 global reanalysis. *Quart. J. Roy. Meteor. Soc.*, **146**, 1999–2049, https://doi.org/10.1002/qj.3803.

Higgins, R. W., and W. Shi, 2001: Intercomparison of the principal modes of interannual and intraseasonal variability of the North American Monsoon System. *J. Climate*, **14**, 403–417, https://doi.org/10.1175/1520-0442(2001)014<0403:IOTPMO>2.0.CO;2.

——, Y. Yao, and X. L. Wang, 1997: Influence of the North American monsoon system on the U.S. summer precipitation regime. *J. Climate*, **10**, 2600–2622, https://doi.org/10.1175/1520-0442(1997)010<2600:IOTNAM>2.0.CO;2.

Highwood, E. J., and B. J. Hoskins, 1998: The tropical tropopause. *Quart. J. Roy. Meteor. Soc.*, **124**, 1579–1604, https://doi.org/10.1002/qj.49712454911.

Hoskins, B. J., and D. J. Karoly, 1981: The steady linear response of a spherical atmosphere to thermal and orographic forcing. *J. Atmos. Sci.*, **38**, 1179–1196, https://doi.org/10.1175/1520-0469(1981)038<1179:TSLROA>2.0.CO;2.

——, and F.-F. Jin, 1991: The initial value problem for tropical perturbations to a baroclinic atmosphere. *Quart. J. Roy. Meteor. Soc.*, **117**, 299–317, https://doi.org/10.1002/qj.49711749803.

——, and M. J. Rodwell, 1995: A model of the Asian summer monsoon. Part I: The global scale. *J. Atmos. Sci.*, **52**, 1329–1340, https://doi.org/10.1175/1520-0469(1995)052<1329:AMOTAS>2.0.CO;2.

——, M. E. McIntyre, and W. Robertson, 1985: On the use and significance of isentropic potential vorticity maps. *Quart. J. Roy. Meteor. Soc.*, **111**, 877–946, https://doi.org/10.1002/qj.49711147002.

Hou, A. Y., and Coauthors, 2014: The Global Precipitation Measurement Mission. *Bull. Amer. Meteor. Soc.*, **95**, 701–722, https://doi.org/10.1175/BAMS-D-13-00164.1.

Hu, Y., and K. K. Tung, 2002: Interannual and decadal variations of planetary wave activity, stratospheric cooling, and Northern Hemisphere annular mode. *J. Climate*, **15**, 1659–1673, https://doi.org/10.1175/1520-0442(2002)015<1659:IADVOP>2.0.CO;2.

Huffman, G. J., and Coauthors, 2018: NASA Global Precipitation Measurement (GPM) Integrated multi-satellitE retrievals for GPM (IMERG). Algorithm Theoretical Basis Doc., version 6, 39 pp., https://gpm.nasa.gov/sites/default/files/2020-05/IMERG_ATBD_V06.3.pdf.

Jin, F., and B. J. Hoskins, 1995: The direct response to tropical heating in a baroclinic atmosphere. *J. Atmos. Sci.*, **52**, 307–319, https://doi.org/10.1175/1520-0469(1995)052<0307:TDRTTH>2.0.CO;2.

Kiladis, G. N., 1998: Observations of Rossby waves linked to convection over the eastern tropical Pacific. *J. Atmos. Sci.*, **55**, 321–339, https://doi.org/10.1175/1520-0469(1998)055<0321:OORWLT>2.0.CO;2.

Lau, K.-M., and H. Lim, 1982: Thermally driven motions in an equatorial β-plane: Hadley and Walker circulations during the winter monsoon. *Mon. Wea. Rev.*, **110**, 336–353, https://doi.org/10.1175/1520-0493(1982)110<0336:TDMIAE>2.0.CO;2.

Liebmann, B., and C. A. Smith, 1996: Description of a complete (interpolated) outgoing longwave radiation dataset. *Bull. Amer. Meteor. Soc.*, **77**, 1275–1277.

Matsuno, T., 1966: Quasi-geostrophic motions in the equatorial area. *J. Meteor. Soc. Japan*, **44**, 25–43, https://doi.org/10.2151/jmsj1965.44.1_25.

Pittman, J. V., and Coauthors, 2007: Transport in the subtropical lowermost stratosphere during the Cirrus Regional Study of Tropical Anvils and Cirrus Layers-Florida Area Cirrus Experiment. *J. Geophys. Res.*, **112**, D08304, https://doi.org/10.1029/2006JD007851.

Ploeger, F., and Coauthors, 2013: Horizontal water vapor transport in the lower stratosphere from subtropics to high latitudes during boreal summer. *J. Geophys. Res.*, **118**, 8111–8127, https://doi.org/10.1002/jgrd.50636.

Popovic, J. M., and R. A. Plumb, 2002: Eddy shedding from the upper-tropospheric Asian monsoon anticyclone. *J. Atmos. Sci.*, **58**, 93–104, https://doi.org/10.1175/1520-0469(2001)058<0093:ESFTUT>2.0.CO;2.

Randel, W. J., and M. Park, 2006: Deep convective influence on the Asian summer monsoon anticyclone and associated tracer

variability observed with Atmospheric Infrared Sounder (AIRS). *J. Geophys. Res.*, **111**, D12314, https://doi.org/10.1029/2005JD006490.

——, K. Zhang, and R. Fu, 2015: What controls stratospheric water vapor in the NH summer monsoon regions? *J. Geophys. Res. Atmos.*, **120**, 7988–8001, https://doi.org/10.1002/2015JD023622.

Sardeshmukh, P. D., and B. J. Hoskins, 1988: The generation of global rotational flow by steady idealized tropical divergence. *J. Atmos. Sci.*, **45**, 1228–1251, https://doi.org/10.1175/1520-0469(1988)045<1228:TGOGRF>2.0.CO;2.

Schneider, T., 2004: The tropopause and the thermal stratification in the extratropics of a dry atmosphere. *J. Atmos. Sci.*, **61**, 1317–1340, https://doi.org/10.1175/1520-0469(2004)061<1317:TTATTS>2.0.CO;2.

——, and C. C. Walker, 2006: Self-organization of atmospheric macroturbulence into critical states of weak nonlinear eddy–eddy interactions. *J. Atmos. Sci.*, **63**, 1569–1586, https://doi.org/10.1175/JAS3699.1.

Schumacher, C., R. A. Houze, and I. Kraucunas, 2004: The tropical dynamical response to latent heating estimates derived from the TRMM Precipitation Radar. *J. Atmos. Sci.*, **61**, 1341–1358, https://doi.org/10.1175/1520-0469(2004)061<1341:TTDRTL>2.0.CO;2.

Simpson, J., R. F. Adler, and G. R. North, 1988: A proposed Tropical Rainfall Measuring Mission (TRMM) satellite. *Bull. Amer. Meteor. Soc.*, **69**, 278–295, https://doi.org/10.1175/1520-0477(1988)069<0278:APTRMM>2.0.CO;2.

Siu, L. W., and K. P. Bowman, 2019: Forcing of the upper-tropospheric monsoon anticyclones. *J. Atmos. Sci.*, **76**, 1937–1954, https://doi.org/10.1175/JAS-D-18-0340.1.

Stensrud, D. J., 2013: Upscale effects of deep convection during the North American monsoon. *J. Atmos. Sci.*, **70**, 2681–2695, https://doi.org/10.1175/JAS-D-13-063.1.

Tang, M., and E. R. Reiter, 1984: Plateau monsoons of the Northern Hemisphere: A comparison between North America and Tibet. *Mon. Wea. Rev.*, **112**, 617–637, https://doi.org/10.1175/1520-0493(1984)112<0617:PMOTNH>2.0.CO;2.

Webster, P. J., 1972: Response of the tropical atmosphere to local, steady forcing. *Mon. Wea. Rev.*, **100**, 518–541, https://doi.org/10.1175/1520-0493(1972)100<0518:ROTTAT>2.3.CO;2.